



Cite this: *RSC Sustainability*, 2025, **3**, 2632

Nonthermal plasma assisted desorption and conversion of captured CO₂ from atmospheric air[†]

Chinwendu Umeojiakor,^a Loukia-Pantzechrula Merkouri,^b Anthony Griffin,^b Melis S. Duyar,^b Zhe Qiang^b and Yizhi Xiang^{b*}^{ad}

CO₂ capture and conversion are essential to mitigate the global climate crisis. However, sorbent regeneration frequently relies on the high-temperature thermal-driven process, making the integration of intermittent renewable energy into the process an inherent challenge. Herein, with a lime-based sorbent model system, we show that an electrified process for the desorption and conversion of captured CO₂ (to CO or CH₄) can be achieved through a non-thermal dielectric-barrier discharge plasma reactor. Specifically, up to 87.7% of captured CO₂ (by CaO from the air) can be converted into CO under the discharge of 10% H₂/Ar at a power of 24.7 W. The reaction can also be tuned for CH₄ production when a dual function material, Ni–Ru CaO/CeO₂–Al₂O₃, or a physical mixture of CaO and a Ru/Al₂O₃ methanation catalyst is employed. The kinetics of such a process are evaluated based on the nonsteady-state semi-batch reactor model. The reactions are identified to be first order for both CO₂ desorption and hydrogenation processes.

Received 4th December 2024
Accepted 24th April 2025

DOI: 10.1039/d4su00768a
rsc.li/rscsus

Sustainability spotlight

To deal with the climate crisis that originated from the greenhouse effect due to the extensive usage of fossil fuels, CO₂ must be captured by a sorbent material both at point of large-scale emission sources and directly from the atmospheric air. The captured CO₂ within sorbent materials needs to be desorption and/or conversion through the high-temperature thermal-driven process, making the integration of intermittent renewable energy into the process an inherent challenge. The current research show that an electrified process, namely, non-thermal dielectric-barrier discharge plasma assisted desorption and conversion of captured CO₂ (to CO or CH₄) by CaO based sorbent from atmospheric air. This work aligns with the UN SDGs 9 (industry, innovation, and infrastructure) and 13 (climate action).

1. Introduction

To meet the energy and chemical demands of modern society, fossil fuels such as coal, petroleum, and natural gas have been used on an unprecedented scale. This extensive usage has resulted in the annual release of more than 37 billion tons of CO₂ into the environment.¹ The increase of CO₂ concentration in the atmosphere has led to a significant climate crisis due to the greenhouse effect, which requires nations to reduce net greenhouse gas emissions by 50–52% in 2030 and reach net-zero emissions no later than 2050.² In order to achieve these targets, applying carbon negative technologies, such as carbon

capture and storage/utilization, is of particular importance. Consequently, CO₂ must be captured by a sorbent material both at the point of large-scale emission sources (such as fossil fuels fired power plants and the iron and steel sectors) and directly from the atmospheric air. The captured CO₂ within sorbent materials must be regenerated through thermal-driven desorption and/or conversion *via* various reactions such as methanation, reverse water-gas-shift, and dry reforming. Sorbent regeneration is the most energy-intensive step during the process, and therefore there is an urgent need to develop alternative regeneration routes with reduced energy use and environmental footprint.^{3–7}

Among various solid sorbent materials, calcium oxide (CaO) has a high CO₂ capture capacity ($\sim 0.78 \text{ gCO}_2/\text{gCaO}$) and is cost-efficient, with estimated capture costs of 26 USD per ton CO₂ according to techno-economic analyses.^{8,9} Additionally, CaO precursors (*e.g.*, natural limestone) are abundant and nontoxic,¹⁰ and as a result, the “calcium looping” (CaL) technology has been identified as a promising alternative to the current amine scrubbing technique for CO₂ (and also SO₂) capture at points of large-scale emission sources.^{10–13} Consequently, CaO as a sorbent has been extensively studied either in an attempt to increase the

^aDave C. Swalm School of Chemical Engineering, Mississippi State University, Mississippi State, MS 39762, USA. E-mail: yxpzb@missouri.edu

^bSchool of Chemistry and Chemical Engineering, University of Surrey, Guildford, GU2 7XH, UK

^cSchool of Polymer Science and Engineering, University of Southern Mississippi, Hattiesburg, MS 39406, USA

^dDepartment of Chemical and Biomedical Engineering, University of Missouri, Columbia, MO 65211, USA

[†] Electronic supplementary information (ESI) available. See DOI: <https://doi.org/10.1039/d4su00768a>



cyclic CO_2 uptake stability,^{14–18} or in conjunction with a transition metal catalyst, forming dual function materials (DFMs), for CO_2 conversion.^{19–25} Besides CO_2 capture at the point of large-scale emission source, the CaL-related process can also be employed to remove CO_2 from the atmosphere (direct air capture, DAC) to compensate for hard-to-decarbonize sectors, such as automobile and aviation. For example, the CaL is in the center of the DAC process using hydroxide solutions, which has been explored by Carbon Engineering Ltd in Canada.²⁶ In such a process, the produced carbonate (e.g., K_2CO_3) after DAC is reacted with $\text{Ca}(\text{OH})_2$ to form CaCO_3 for hydroxide (KOH) regeneration; then CaCO_3 is separated and calcined to CaO , which is finally rehydrated to $\text{Ca}(\text{OH})_2$. Additionally, DAC configurations that only use CaO have also been studied.^{6,27}

During the CaL processes, a common critical step is the CaO regeneration either through calcination of CaCO_3 at a high temperature of up to 950 °C (typically achieved in a gas burner furnace with liquefied petroleum gas as the fuel²⁸) or reaction of the captured CO_2 with H_2 or CH_4 (at relatively lower temperatures). The high temperature required for the CaO regeneration makes the CaL processes highly energy intensive. Alternative heating methods, such as concentrated solar radiation, have been employed for CaO regeneration through decomposition or CH_4 reforming.^{29,30} However, a high reaction temperature is still required, and the deactivation of sorbent due to sintering remains significant. Unlike conventional thermal radiation, the dielectric barrier discharge (DBD) plasma offers a unique way to inject energy (ideally from renewable electricity) into a reacting system by generating activated species, such as hot electrons, electronically and vibrationally excited species, ions, and radicals. The integration of plasma with heterogeneous catalytic processes is an emerging technology for power-to-X, capable of CO_2 conversion through CH_4 reforming,^{31–39} hydrogenation,^{40–42} and direct decomposition.^{43–46} While literature precedents show promising reaction results in gas-phase CO_2 conversion, the nonthermal plasma-driven conversion of captured CO_2 has only been studied with hydrotalcite as the sorbent by Li *et al.*,^{47,48} a similar study with CaO as the sorbent has not been investigated, likely due to the high power requirement owing to the high thermal stability of CaCO_3 .

Herein, we show an electrified process using the DBD plasma to drive the conversion of CO_2 captured by the CaO -based sorbent into CO or CH_4 . In such a process, the plasma-activated species, such as the hot electrons, ions (Ar^+ and H_2^+), and radicals ($\cdot\text{H}$) from the discharge of the H_2/Ar mixture, can interact with the surface of the CaCO_3 , converting the captured CO_2 into CO at high conversion. The plasma reactor was insulated to reduce the heat loss, known as “adiabatic” plasma reactor,⁴⁹ achieving efficient CO_2 desorption and conversion at the power of 25–28 W. This study demonstrates non-thermal plasma-assisted desorption and conversion of CO_2 captured by CaO -based sorbent at significantly lower temperatures in contrast to traditional thermal regeneration method, reducing energy costs and sorbent material sintering. CO produced from this process can be coupled with Fischer–Tropsch synthesis, leading to a representative power-to-liquid process. Additionally, the product selectivity can be tuned

from CO to CH_4 when a catalytic methanation active site is incorporated into the sorbent, forming a dual-function material, or when a physical mixture of a CaO sorbent and a separate methanation catalyst ($\text{Ru}/\text{Al}_2\text{O}_3$) is used, leading to a typical power-to-gas process. The plasma-assisted process can also be employed for converting captured CO_2 by other sorbents and dual-function materials, providing renewable energy-driven alternative carbon capture and utilization techniques.

2. Experimental

2.1 Samples preparation

The CaO , 10 wt% MgO/CaO (Mg_{10}CaO), 10 wt% ZrO_2/CaO (Zr_{10}CaO), 10 wt% Ni (Ni_{10}CaO), and 5 wt% $\text{Ni} + 5$ wt% MgO ($\text{Ni}_5\text{Mg}_5\text{CaO}$) samples were prepared through oxalate method with $\text{H}_2\text{C}_2\text{O}_4 \cdot 2\text{H}_2\text{O}$ (≥99.5%, Chemsavers), $\text{Ca}(\text{OH})_2$ (≥98%, Aldrich Chemical Company, Inc), $\text{Mg}(\text{NO}_3)_2 \cdot 6\text{H}_2\text{O}$, $\text{Ni}(\text{NO}_3)_2 \cdot 6\text{H}_2\text{O}$ (≥98%, Millipore Sigma), and/or ZrCl_4 (≥99.5%, Strem Chemicals) as the precursors. Based on the desired weight ratio, these precursors were measured and placed in different beakers. The amount of oxalic acid was 20% excess than the stoichiometric amount necessary for precipitating all metal cations in solution to ensure the metal oxalate formation is not limited by oxalate concentration. Specifically, the powder of $\text{Ca}(\text{OH})_2$ and a solution of magnesium nitrate, nickel nitrate, or zirconium chloride were added to the solution of oxalic acid under stirring. The slurry was stirred for 2 h at a speed of 500 rpm and room temperature and then kept in the beaker overnight. Finally, the slurry was centrifuged at 4000 rpm to separate the precipitate. The collected sample was dried in an oven overnight at 100 °C and calcined at 850 °C (ramping at 10 °C min^{−1}) under static air for 4 h. The sample was pelletized, then crushed and sieved to obtain a size fraction between 125 and 250 μm for characterization and DAC study.

The Ni – Ru $\text{CaO}/\text{CeO}_2\text{–Al}_2\text{O}_3$ DFM was prepared by sequential impregnation.²¹ Firstly, $\text{Ca}(\text{NO}_3)_2 \cdot 4\text{H}_2\text{O}$ (Sigma Aldrich) was mixed with the $\text{CeO}_2\text{–Al}_2\text{O}_3$ support (SCFa-160 Ce20 Puralox, Sasol) and deionized water. The resulting suspension was mixed using a magnetic stirrer at a speed of 500 rpm and room temperature, and then, a rotary evaporator was used to remove the excess water under reduced pressure. The mixture was dried overnight at 120 °C and calcined at 400 °C (5 °C min^{−1} ramp and a 4 h hold). After that, the $\text{CaO}/\text{CeO}_2\text{–Al}_2\text{O}_3$ was mixed with excess water, and the required amounts of $\text{Ni}(\text{NO}_3)_2 \cdot 6\text{H}_2\text{O}$ (Acros Organics) and $\text{Ru}(\text{NO})(\text{NO}_3)_3$ solution (1.5 w/v Ru , Alfa Aesar). After mixing all together with a magnetic stirrer a speed of 500 rpm and room temperature, the excess water was removed using a rotary evaporator, and the resulting powder was dried overnight at 120 °C and calcined at 500 °C (5 °C min^{−1} ramp, 3 h soak). The obtained DFM had 15 wt% Ni , 1 wt% Ru , and 10 wt% CaO on the $\text{CeO}_2\text{–Al}_2\text{O}_3$ support (20–80 wt%).

The $\text{Ru}/\text{Al}_2\text{O}_3$ (5 wt% nominal loadings) was prepared by impregnation followed by wet reduction using NaHB_4 . Typically, 2 g of Al_2O_3 (Inframal Advanced Materials) was first mixed with 10 mL of RuCl_3 (Sigma-Aldrich) aqueous solution (0.01 g_{Ru} mL^{−1}). The resulting suspension was mixed with a magnetic stirrer at a speed of 500 rpm and room temperature for 3 h, then 0.373 g of NaHB_4 (98%, Thermo Scientific) was dissolved in



around 2 mL deionized water and added dropwise to the suspension and stirred at room temperature for 1 h. The slurry was finally centrifuged to collect the solid samples, which were dried in an oven overnight at 100 °C without calcination.

2.2 Sample characterization

X-ray powder diffraction (XRD) patterns were collected on a Rigaku Ultima III X-ray diffractometer with monochromatic Cu K α radiation (154.06 pm, 40 kV, and 44 mA) in the range of 2 θ from 10° to 60° with a scan speed of 4° min⁻¹. Scanning Electron Microscope (SEM) of the sample was measured using a JEOL 6500F SEM and Zeiss Supra 40 SEM. Nitrogen adsorption/desorption isotherms were measured in a Micromeritics Tristar II 3020 analyzer at 77 K. The sample was degassed at 300 °C under vacuum for 16 h before N₂ adsorption/desorption measurement. The surface areas were determined by Brunauer–Emmett–Teller (BET) analysis. *In situ* diffuse reflectance infrared Fourier transform spectroscopy (DRIFTS) spectra of the CaO under the DAC conditions were collected on a Thermo Scientific Nicolet i20 FTIR spectrometer equipped with a liquid-nitrogen-cooled mercury-cadmium-telluride detector and a Praying Mantis high-temperature *operando* reaction chamber (Harrick Scientific Products Inc.) with calcium fluoride windows. The spectra were recorded at a resolution of 4 cm⁻¹ with accumulations of 32 scans per min under 30 mL min⁻¹ of atmospheric air (introduced using an aquarium air pump, and the flow rate was controlled with a Brooks mass flow controller).

2.3 DAC and plasma-driven CO₂ desorption and conversion

Direct air capture (DAC) was achieved by passing atmospheric air through the sorbent under ambient conditions. The sorbent samples containing Ni and Ru were pre-reduced under 30 mL min⁻¹ 10% H₂/Ar at 600 °C (ramping at 10 °C min⁻¹) for 1 h before DAC. Specifically, 0.5 g of sorbent was first loaded into a 3/8-inch quartz tube with an inner diameter of 7 nm. Then 200 mL min⁻¹ of atmospheric air was passed through the tube for at least 24 h to achieve a saturated CO₂ capture on the sorbent. The atmospheric air was introduced using an aquarium air pump and the flow rate was controlled with a Brooks mass flow controller.

The plasma-driven desorption and conversion of captured CO₂ was performed in a coaxial DBD quartz reactor, which has an inner diameter of 4 mm and an outer diameter of 1/4".^{50,51} Specifically, a 6 cm long stainless steel mesh (20 mesh) was employed as the outer (ground) electrode and wrapped tight around the quartz tube. A K-type thermocouple was attached to the steel mesh electrode for external reactor temperature measurement immediately after turning off the plasma. The outer electrode and thermocouple were wrapped with a ceramic fiber with a 1 cm thickness for insulation, known as “adiabatic” plasma reactor.⁴⁹ Such an insulated electrode minimizes the heat loss from the electrode, self-heating the plasma reactor up to 500 °C (dependent upon the applied power) without an external heat supply.^{49,52} A 1/16" tungsten electrode was inserted at the center of the reactor and acted as the inner high-voltage electrode. The discharge volume of the DBD reactor is 0.64 cm³ without loading the sorbent/catalyst. The DBD plasma was

generated using a PMV500 high-voltage AC power source with an applied voltage of 9–15 kV and a frequency of 22 kHz. The applied voltage was measured by a Tektronix P6015A high-voltage probe connected to a Tektronix MDO32 3-BW-100 oscilloscope, and the voltage across a 10 nF capacitor (U_C) was measured by the same oscilloscope with a TPP0250 voltage probe. The power input of the plasma was calculated based on the area inside the charge-voltage (Q–V) Lissajous curves,³¹ where the voltage V refers to the applied voltage and the charge Q can be calculated from the voltage drop across the external capacitor (capacitance 10 nF).

$$Q = C_{\text{capacitor}} \times U_C \quad (1)$$

Typically, 0.1 g of the sample (pre-adsorbed with CO₂ through DAC) was loaded into the reactor. The reactor inlet gas, either Ar (for desorption) or 10% H₂/Ar (for CO₂ hydrogenation), was controlled using a Brooks mass flow controller. The reactor outlet was measured by an online Agilent 5973 mass spectrometer (MS, equipped with MS Sensor 2.0 software, Diablo Analytical, Inc). Specifically, *m/z* = 15, *m/z* = 28, *m/z* = 44, and *m/z* = 40 were measured. The intensity of the *m/z* signal (*I_{m/z}*) is then converted to the intensity of each molecule (*I_{molecule}*) based on the quantitative calibration, namely, *I_{Ar = *I₄₀*, *I_{CO₂}*}* = *I₄₄*, *I_{CH₄}* = *I₁₅*, and *I_{CO}* = *I₂₈* - 0.0495 × *I₄₄*. The MS signal intensities of Ar, CO₂, CO, and CH₄ were converted to partial pressure based on external standard calibration. A more detailed method for quantitative MS analysis can be found in the ref. 53.

The partial pressure was finally calculated to each molecule's mole flow rate (mol min⁻¹) based on the ideal gas equation (*P_iv_{tot = *F_iRT*}*), where *P_i* is the partial pressure of selected molecules (Pa), *v_{tot}* is the total volumetric flow rate (mL min⁻¹), *F_i* is the mole flow rate (mol min⁻¹), *R* is the ideal gas constant (J mol⁻¹ K), and *T* is the temperature (K).

The desorption rates of CO₂, CO, and CH₄ were calculated by normalizing *F_i* with the weight of the sample (pre-adsorbed with CO₂ through DAC).

The time-dependent desorption rates were integrated to obtain the total desorption of CO₂ (*n_{CO₂}*), CO (*n_{CO}*), and CH₄ (*n_{CH₄}*). The composition of each species was calculated based on the normalized total desorption amounts. CO₂ conversion was calculated based on eqn (2).

$$X = \frac{n_{\text{CO}} + n_{\text{CH}_4}}{n_{\text{CO}} + n_{\text{CH}_4} + n_{\text{CO}_2}} \quad (2)$$

The selectivity of CO and CH₄ were then calculated based on eqn (3).

$$S_i = \frac{n_i}{n_{\text{CO}} + n_{\text{CH}_4}} \times 100\% \quad (3)$$

3. Results and discussion

3.1. CO₂ capture by CaO

The nanosized CaO model sorbent (see Fig. S1† for a typical SEM image) was prepared through the thermal decomposition

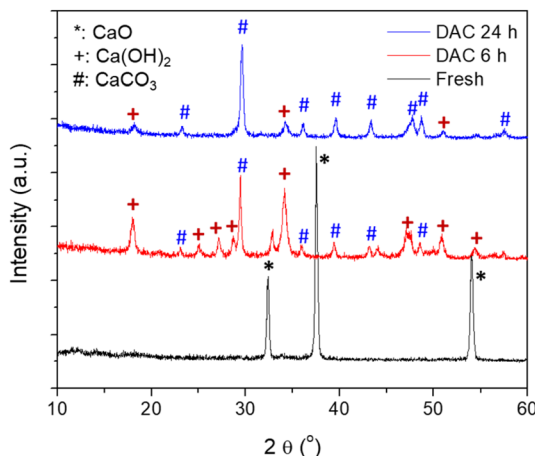


Fig. 1 XRD patterns of the fresh CaO and the CaO subjected to DAC for 6 h and 24 h, respectively.

of Ca oxalate. The N_2 physisorption results of the Ca oxalate and the fresh CaO showed BET surface areas of 16.1 and $56.1\text{ m}^2\text{ g}^{-1}$, respectively (see Fig. S2†). The XRD patterns of the fresh, *i.e.*, as obtained, CaO and the CaO samples after DAC for 6 h and 24 h, respectively, are shown in Fig. 1. It was seen that the CaO sorbent turned into a mixture of CaCO_3 and $\text{Ca}(\text{OH})_2$ after DAC for 6 h (see also Fig. S3†) and almost pure CaCO_3 after 24 h (see also Fig. S4†). The XRD patterns shown in Fig. 1 support that CO_2 capture by the CaO could be achieved by the DAC method. The BET surface area of the CaO sample decreased to $38.7\text{ m}^2\text{ g}^{-1}$ (see Fig. S2†) after capturing CO_2 due to the volume expansion and mass increase after converting CaO into CaCO_3 . Noteworthily, the BET surface area increased to $57.8\text{ m}^2\text{ g}^{-1}$ (almost identical to the fresh CaO) after 1 cycle of the CO_2 capture, followed by plasma-assisted hydrogenation of the captured CO_2 . The presence of $\text{Ca}(\text{OH})_2$ in the sample after DAC for 6 h suggests that moisture played a critical role in CO_2 capture: CaO first reacted with moisture to form $\text{Ca}(\text{OH})_2$ intermediate, which then reacted with CO_2 to form CaCO_3 . The formation of $\text{Ca}(\text{OH})_2$ as the intermediate was also evidenced by the *in situ* DRIFTS study. As shown in Fig. S5,† the immediate appearance of the OH vibrations (at wavenumbers of around 3640 cm^{-1}) after exposure to air indicated the fast formation of $\text{Ca}(\text{OH})_2$ from CaO and moisture during the DAC process. Consequently, the moisture level in the air could strongly influence the rate of DAC. Because this paper focuses on the plasma-assisted desorption and conversion of captured CO_2 by the CaO-based sorbent, a more detailed influence of moisture on the DAC will not be discussed.

3.2. Plasma-assisted desorption/conversion of captured CO_2 : proof-of-concept

The CaO model sorbent after the DAC was subjected to plasma-assisted desorption and conversion (*i.e.* hydrogenation) of the captured CO_2 under either pure Ar or 10% H_2/Ar , respectively. Fig. 2(a) and (b) show the electrical signals and Q – V Lissajous curve of the H_2/Ar discharge employed for the proof-of-concept study. It can be observed from Fig. 2(a) that the applied peak-to-

peak voltage was 14.8 kV at the frequency (f) of 22.3 kHz (period time $t = 1/f = 45\text{ }\mu\text{s}$), and the peak-to-peak voltage drop across the external capacitor was 35 V under the applied voltage and reaction conditions. The Q – V Lissajous curve shown in Fig. 2(b) was between a parallelogram and oval shape, which is a typical discharge behavior for a coaxial dielectric barrier discharge reactor. The discharge power was calculated to be 28.3 W based on the area of the Lissajous curves. The electrical signals and Q – V Lissajous curve of the Ar discharge were almost identical to that of 10% H_2/Ar , except that the Ar discharge showed a slightly lower charge at the same applied voltage. According to the Lissajous curve, the power of Ar plasma was around 25.2 W, which was slightly lower than the plasma of 10% H_2/Ar .

The reaction/desorption behaviors of the captured CO_2 by CaO assisted by the plasma of 10% H_2/Ar are shown in Fig. 2(c) and (e). It was demonstrated that the desorption and conversion of the captured CO_2 could be achieved by the DBD plasma without an external heat supply. As shown in Fig. 2(c), desorption of CO and CO_2 was observed, whereas desorption of CH_4 was negligible during the plasma treatment. The desorption rates of CO_2 , CO, and CH_4 mainly showed broad peaks during the reaction/desorption process. Initially, the rates of desorption/reaction increased due to the increase in the reactor temperature. The rates then started decreasing when the temperature reached the maximum due to the decreased CaCO_3 concentration. A small peak within the first 5 min after turning on the plasma can be found. These initial peaks are ascribed to the reaction/desorption of the chemisorbed CO_2 rather than the decomposition of CaCO_3 . The main desorption peaks for CO and CO_2 were broad, and the full width at half maximum (FWHM) was 15.9 and 13.2 min, respectively. The maximum rates (peak of the desorption rate curves) of CO and CO_2 desorption were 353 and $180\text{ }\mu\text{mol}(\text{g}^{-1}\text{ min}^{-1})$ and were achieved after 15.5 and 18 min, respectively. The total desorption of CO and CO_2 took around 40 min under the applied plasma conditions (14.8 kV and 28.3 W), indicating a relatively slow decomposition process due to the high thermal stability of the CaCO_3 . For comparison, temperature-programmed desorption (TPD) profiles of the CaO (after DAC) are shown in Fig. S6.† It was observed that the desorption of CO and CO_2 started at temperatures around $600\text{ }^\circ\text{C}$, and total desorption of CO and CO_2 was achieved by $800\text{ }^\circ\text{C}$.

By integrating the desorption rates (Fig. 2(c)), the cumulative desorption of CO, CO_2 , and CH_4 per unit mass of “ CaCO_3 ” (CaO after DAC) was obtained. As shown in Fig. 2(e), the cumulative CO and CO_2 desorption were 5.9 and 2.7 mmol g^{-1} , respectively, whereas the total CH_4 desorption was only 0.28 mmol g^{-1} . These results corresponded to a composition of 66.6% CO, 30.2% CO_2 , and 3.2% CH_4 , namely, 70% conversion of the captured CO_2 and 95.5% selectivity toward CO. The sum desorption of CO, CO_2 , and CH_4 was around 8.9 mmol g^{-1} . Assuming CaO was fully converted into CaCO_3 (based on the XRD results) after the DAC, 1 g of CaCO_3 could release 10 mmol of CO_2 , which is slightly higher than the sum desorption of CO, CO_2 and CH_4 , most likely due to the presence of moisture in the sample after the DAC. Noteworthily, the sum desorption of CO, CO_2 , and CH_4 during the TPD of the CaO (after DAC) was 9.1 mmol g^{-1} (see Fig. S6†), almost identical to the plasma-



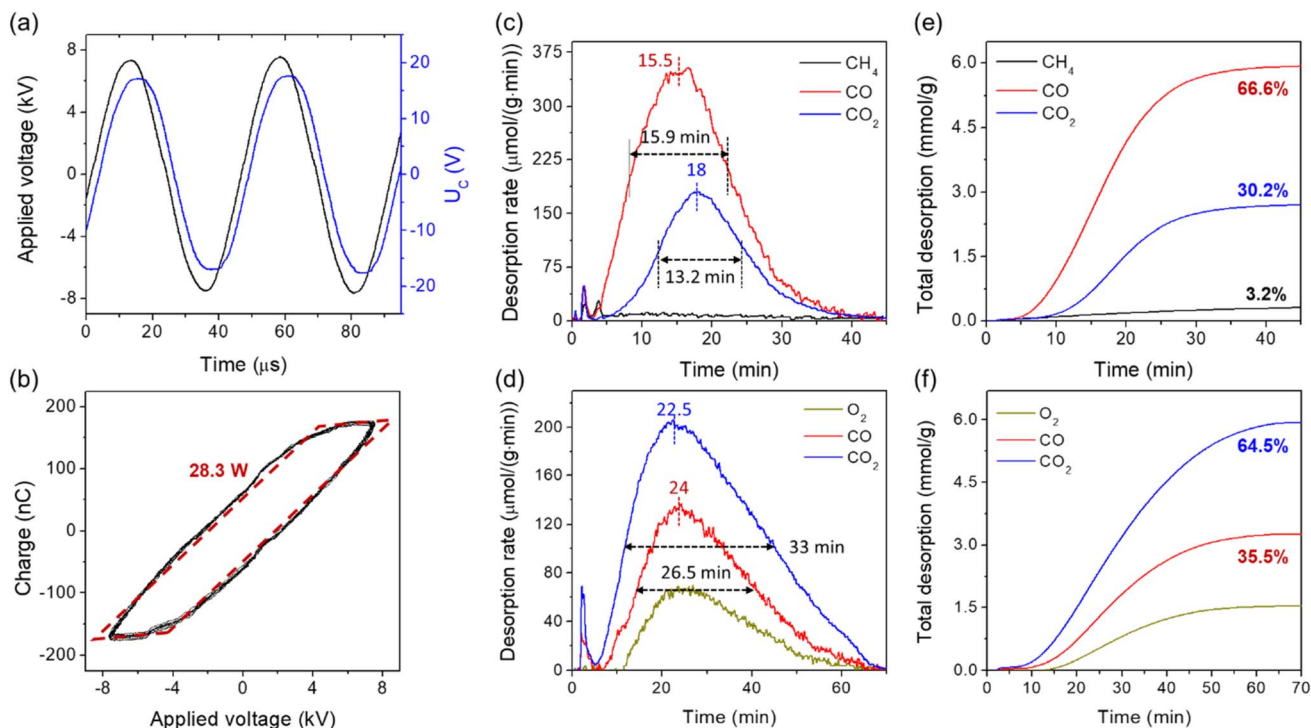


Fig. 2 Electric signals and reaction/desorption behaviors during plasma-assisted desorption and conversion of CO_2 captured by CaO . (a) Electrical signals of the H_2/Ar discharge; (b) Q-V Lissajous curve of the discharge; (c) and (d) desorption rates under H_2/Ar and Ar plasma, respectively, and (e) and (f) cumulative total desorption of CO_2 , CO , and CH_4 under H_2/Ar and Ar plasma, respectively. Reaction conditions: 0.1 g of "CaCO₃" (CaO after DAC for 24 h), 10% H_2/Ar 30 mL min⁻¹ and power of 28.3 W for (c) and (e), Ar 30 mL min⁻¹ and power of 25.2 W for (d) and (f).

assisted process, indicating that all captured CO_2 had been desorbed/converted by the plasma. Moreover, the conversion of captured CO_2 into CO during the TPD was only 51%, significantly lower than the plasma-assisted process. In turn, these results suggest the plasma-assisted process can be more efficient for converting CO_2 into CO than the thermal process.

Besides the plasma of 10% H_2/Ar , desorption and conversion of the captured CO_2 (by CaO) could also be achieved with Ar plasma. As shown in Fig. 2(d), desorption of CO and O_2 was identified in the absence of H_2 , indicating that the desorbed CO_2 was decomposed to CO and O_2 ($2\text{CO}_2 \leftrightarrow 2\text{CO} + \text{O}_2$). In contrast to the 10% H_2/Ar plasma, the desorption rates for CO_2 and CO decreased in the absence of H_2 . Specifically, the FWHM for the desorption of CO_2 and CO was 33 and 26.5 min, respectively, and the maximum rates of CO_2 and CO desorption were 203 and 133 $\mu\text{mol} (\text{g}^{-1} \cdot \text{min}^{-1})$, which were achieved after 22.5 and 24 min, respectively. Additionally, the total desorption of CO and CO_2 lasted approximately 70 min. The cumulative total desorption of CO_2 and CO were 5.93 and 3.26 mmol g^{-1} , respectively, corresponding to 35.5% conversion of the captured CO_2 (see Fig. 2(f)). The significantly decreased rate of desorption and CO_2 conversion under the Ar plasma was due to (1) the decreased plasma (25.2 W *versus* 28.3 W) under the same applied voltage and (2) the absence of highly active hydrogen-related species such as $\bar{\text{H}}$ and H_2^+ . Therefore, using an H_2 -containing plasma can be considered as a more effective way to regenerate CaO than Ar plasma.

3.3. Influence of second metal/metal oxide

The results discussed above demonstrated the feasibility of both 10% H_2/Ar and Ar plasma-assisted processes for desorption/conversion of captured CO_2 by CaO . The influence of a second metal/metal oxide doping in the CaO sorbent on the process was investigated only under the 10% H_2/Ar considering the higher desorption rate and CO_2 conversion. As shown in Fig. 3, the influence of doping the CaO sorbent with 10 wt% Ni (Ni_{10}CaO), 10 wt% ZrO_2 (Zr_{10}CaO), 10 wt% MgO (Mg_{10}CaO), and 5 wt% Ni + 5 wt% MgO ($\text{Ni}_5\text{Mg}_5\text{CaO}$) has been selected for investigations, considering the potential of enhancing the stability of the CaO and/or desorption rate by adding these species. It was found that the presence of all those metals/metal oxides decreased the rate of desorption, as indicated by reducing the maximum desorption rate shown in Fig. 3(a) and increased FWHM time shown in Fig. 3(d). Nonetheless, the total desorption of $\text{CO} + \text{CO}_2 + \text{CH}_4$ almost remained unchanged (Fig. 3(b)), indicating that the DAC capacity of the doped CaO for CO_2 was not affected. Specifically, the maximum desorption rate decreased from $>500 \mu\text{mol} (\text{g}^{-1} \cdot \text{min}^{-1})$ for CaO to $<350 \mu\text{mol} (\text{g}^{-1} \cdot \text{min}^{-1})$ for both Mg_{10}CaO and Zr_{10}CaO . Additionally, the FWHM time increased from 15.5 min for CaO to >30 min for both Mg_{10}CaO and Zr_{10}CaO (and completed desorption took up to 70 min). The decreased desorption rate of the Mg_{10}CaO and Zr_{10}CaO , however, was associated with slightly enhanced CO_2 conversion as shown in Fig. 3(c).



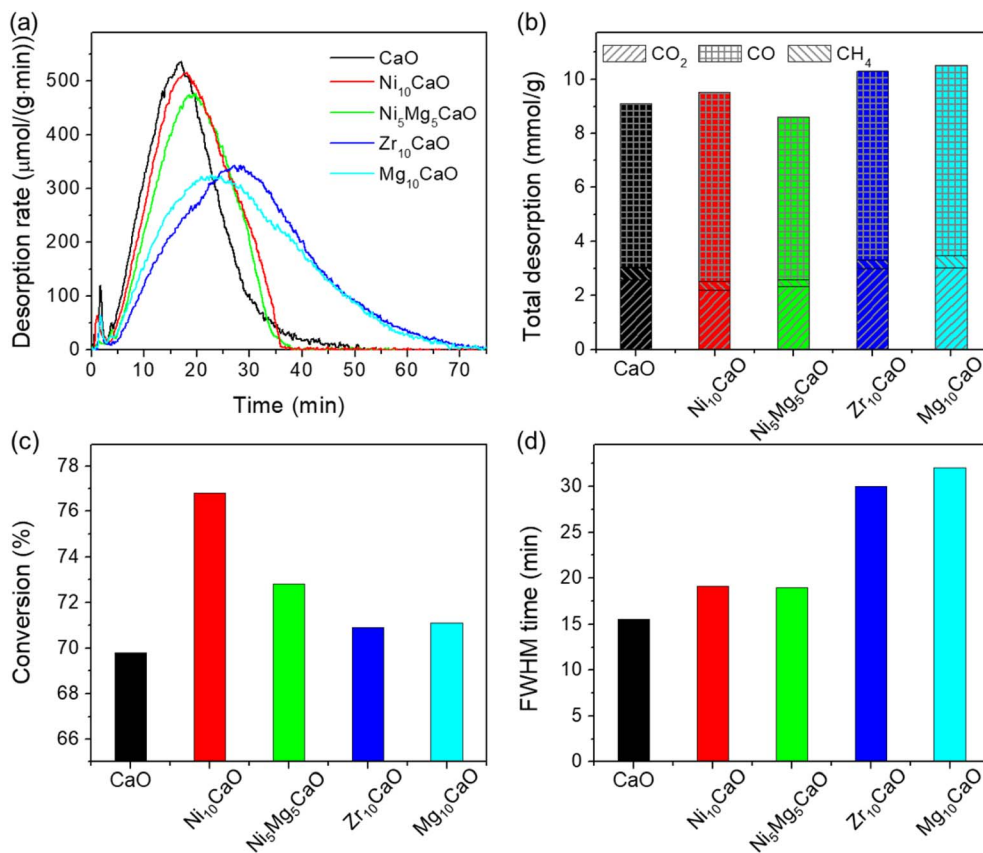


Fig. 3 Influence of second metal/metal oxide on the reaction/desorption behaviors. (a) Desorption rates of CO + CO₂ + CH₄, (b) cumulative total desorption of CO + CO₂ + CH₄, (c) CO₂ conversion, and (d) FWHM time. Reaction conditions: 0.1 g of sample (after DAC for 24 h), 10% H₂/Ar 30 mL min⁻¹, plasma power 28.3 W. More detailed results can be found in Fig. S7.†

While the metal oxide doping decreased the rate of desorption, doping the CaO with metal (Ni) is found to have a negligible influence on the desorption rate. The maximum desorption rate of Ni₁₀CaO was almost identical to that of CaO, and the FWHM time was only slightly increased. Interestingly, the presence of Ni enhanced the desorption rate when the Ni₅Mg₅CaO was compared with the Mg₁₀CaO. The former showed a maximum desorption rate of 474 μmol (g⁻¹·min⁻¹) and an FWHM time of 19 min, whereas the maximum rate and FWHM time of the Ni₅Mg₅CaO were 320 μmol (g⁻¹·min⁻¹) and 32 min. Even though the total desorption of all the studied materials remained almost the same, the presence of Ni increased the CO₂ conversion rate (into CO) compared to the pure CaO sample as shown in Fig. 3(c). Nearly 70% of CO₂ was converted over the CaO (without Ni), but the conversion increased to 77% for the Ni₁₀CaO. The conversion decreased to 73% with decreasing Ni loading to 5 wt% for Ni₅Mg₅CaO. Indeed, the Ni–CaO composite-based material has been widely employed as a dual-function material for CO₂ capture and conversion based on conventional thermal processes.^{24,25,54–56} In this work, we demonstrate that the catalytic function of the Ni (and other transition metals) can also be achieved during the proposed plasma-assisted processes. Noteworthily, while Ni has been considered as a typical methanation catalyst, the formation of CH₄ was negligible under the present conditions, most

likely due to the different mechanisms in the plasma catalysis in contrast to conventional thermal catalysis.

3.4. Tuning the selectivity from CO to CH₄

While Ni doping showed lower CH₄ selectivity, we further discovered that a Ru site could favor the formation of CH₄ under plasma-assisted conditions. The formation of CH₄ was achieved through either physically mixing a Ru/Al₂O₃ methanation catalyst with the CaO-based sorbent or using directly a Ru-containing dual-function material, such as Ni–Ru CaO/CeO₂–Al₂O that has been previously studied by the thermal-assisted process.²¹ As shown in Fig. 4(a), a significant amount of CH₄ was formed by mixing 0.1 g of Zr₁₀CaO sorbent with only 0.02 g of Ru/Al₂O₃ (Ru loading 4 wt%). Based on the cumulative total desorption (see Fig. 4(b)), the total CH₄, CO, and CO₂ desorption were 2.0, 3.8, and 3.2 mmol g⁻¹, respectively. Those corresponded to a composition of 22.2% CH₄, 42.3% CO, and 35.5% CO₂, namely, 64.5% conversion of the captured CO₂ and 34.5% selectivity of CH₄ (CH₄ selectivity increased nearly 7 times in contrast to Zr₁₀CaO only). We note that the selectivity of CH₄ could have been further enhanced by increasing the loading of the Ru/Al₂O₃ and decreasing the sorbent loading, which, however, would have decreased the capacity of the unit volume of the plasma reactor. Additionally, the presence of Ru/Al₂O₃

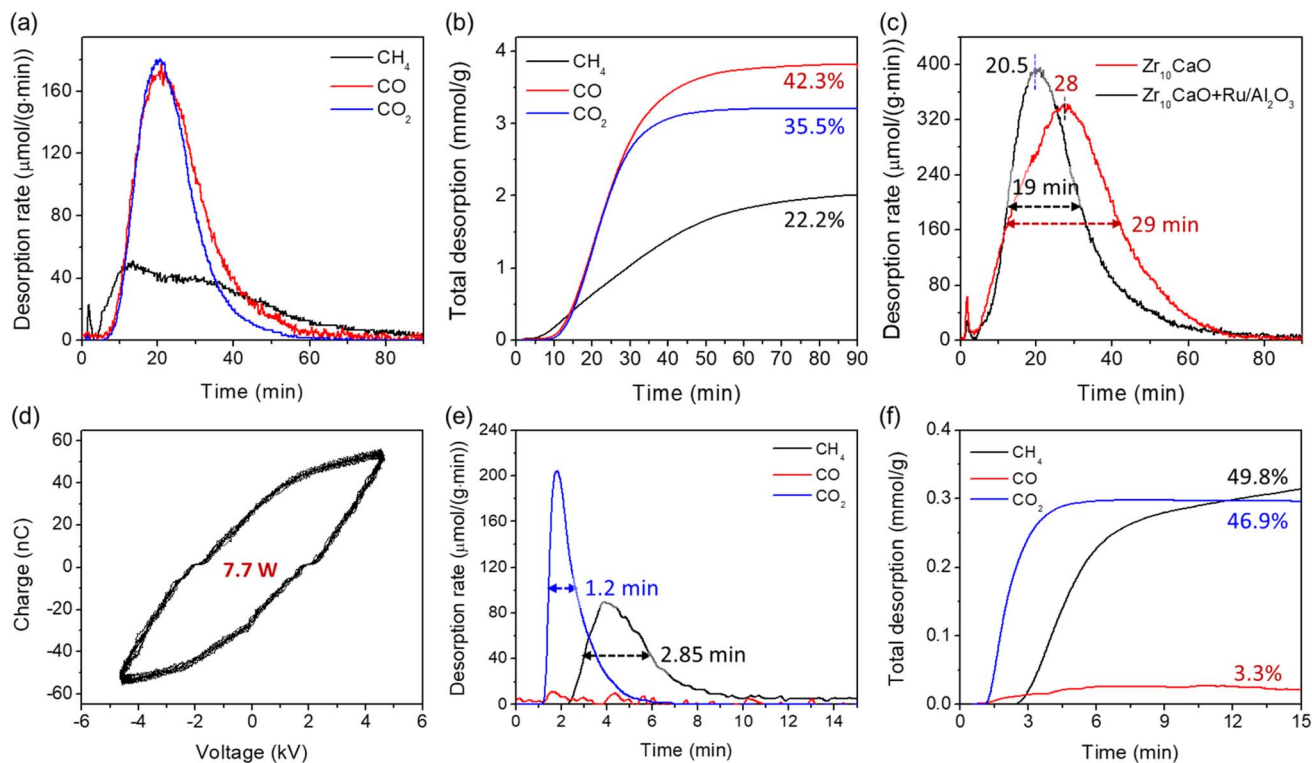


Fig. 4 Results demonstrated the formation of CH_4 as the main product. (a) and (b) desorption rate and total desorption of CH_4 , CO , and CO_2 from $0.1\text{ g Zr}_{10}\text{CaO}$ when mixed with $0.02\text{ g Ru/Al}_2\text{O}_3$ (Ru loading 4 wt%); (c) difference in total C desorption from $0.1\text{ g Zr}_{10}\text{CaO}$ with and without $\text{Ru/Al}_2\text{O}_3$; (d)–(f) results related to $\text{Ni-Ru CaO/CeO}_2\text{-Al}_2\text{O}$ dual-function material. Reaction conditions: 0.1 g of sample (after DAC for 24 h), 10% H_2/Ar 30 mL min^{-1} , plasma power 28.3 W for (a)–(c) and 7.7 W for (e)–(f).

also enhanced the rate of CO_2 desorption since the maximum desorption rate increased, and both peak and FWHM times decreased (see Fig. 4(c)).

Gratifyingly, when a Ru-containing dual-function material, namely $\text{Ni-Ru CaO/CeO}_2\text{-Al}_2\text{O}$, was used for CO_2 DAC and conversion by the plasma, the selectivity to CH_4 increased and the power requirement decreased. As shown in Fig. 4(d), the power calculated from the Q - V Lissajous curve was only 7.7 W in order to desorb/convert the captured CO_2 by the $\text{Ni-Ru CaO/CeO}_2\text{-Al}_2\text{O}$, signifying a *ca.* 72% power reduction compared with the bulk CaO sample. Moreover, the desorption was significantly faster in contrast to the pure or doped CaO . It is illustrated from Fig. 4(e) that the FWHM times for CO_2 and CH_4 desorption were only 1.2 and 2.85 min, respectively, and complete desorption was achieved within 10 min, which was 4 times lower than pure CaO . Over the $\text{Ni-Ru CaO/CeO}_2\text{-Al}_2\text{O}$ dual-function material, CO_2 was captured through weak chemisorption rather than bulk chemisorption/conversion of CaO into CaCO_3 .²¹ The activation energy for the CO_2 desorption/weak chemisorption is significantly lower than that for bulk CaCO_3 decomposition (above 200 kJ mol^{-1}),⁵⁷ which can explain the particularly short reaction time. Moreover, it was also possible that the proximity of the adsorption and catalytic sites in the $\text{Ni-Ru CaO/CeO}_2\text{-Al}_2\text{O}$ played a role in its enhanced performance since the adsorbent and catalyst were impregnated together rather than being only physically mixed. Consequently, the rate of CO_2 desorption and conversion under

the plasma conditions significantly increased. Based on the cumulative total desorption (see Fig. 4(f)), the total CH_4 , CO , and CO_2 desorption were 0.31 , 0.02 , and 0.3 mmol g^{-1} , respectively. The outlet stream had a composition of 49.8% CH_4 , 3.3% CO , and 46.9% CO_2 , while 53.1% conversion of the captured CO_2 and 94% selectivity of CH_4 were also achieved. In contrast to the results of CaO and Ni_{10}CaO sorbents, we conclude that Ru played a significant role in CH_4 formation. Similar to the conventional thermal catalytic CO_2 methanation over the Ru/CeO_2 -based catalyst, we expect that both CO and HCOO^* intermediates⁵⁸ could be involved in CH_4 formation under the plasma conditions. Noteworthily, the $\text{Ni-Ru CaO/CeO}_2\text{-Al}_2\text{O}$ dual-function material employed in this study has been extensively characterized previously,^{21,59} therefore, this paper did not discuss the characterization results of the $\text{Ni-Ru CaO/CeO}_2\text{-Al}_2\text{O}$ sample.

3.5. Kinetics

The above discussion about the FWHM time and the maximum peak desorption rate only provided a qualitative overview of the desorption/conversion activities. Here, an apparent kinetic model was developed based on the molar balance of the reactor and the desorption data obtained over the pure CaO model sorbent. Reactions (i)–(v) could be involved during the plasma (10% H_2/Ar) assisted desorption/conversion process. Since $\text{CaO}\cdot\text{CO}_2$ was not under steady-state but H_2 was under steady-



state flow during the process, the plasma reactor was considered as a “semi-batch” reactor.



Noteworthily, the formation of CO and CH₄ according to reactions (iv) and (v) were negligible in contrast to reactions (i)–(iii) because of the low CO₂ partial pressure (typically <1.5 kPa) and high space velocity (18 000 mL (g⁻¹ h⁻¹)) during the reaction process. Therefore, reactions (iv) and (v) were not considered during the kinetics analysis. The molar balance of the “semi-batch” reactor can be expressed as:

$$-\frac{dn_{\text{CO}_2}}{dt} = (r_1 + r_2 + r_3)V \quad (4)$$

where n_{CO_2} is the total mole number of captured CO₂ and r_1 , r_2 , and r_3 are the rates of reactions (i)–(iii), respectively.

The reaction rates in eqn (4) can be expressed by the power law model:

$$r_1 = k_1 C_{\text{CO}_2}^\alpha \quad (5)$$

$$r_{j(j=2 \text{ or } 3)} = k_j' C_{\text{CO}_2}^\alpha \quad (6)$$

where k_1 is the rate constant of reaction (i), and $k_j' (j=2 \text{ or } 3)$ ($k' = kP_{\text{H}_2}^\beta$, where P_{H_2} is the partial pressure of H₂, fixed at 0.1 atm) is the apparent rate constant of reaction (ii) and (iii). C_{CO_2} is the concentration of CO₂, and α is the reaction order. Combination of molar balance (eqn (4)) with rate equations (eqn (5) and (6)) yield:

$$-\frac{dC_{\text{CO}_2}}{dt} = (k_1 + k_2' + k_3') C_{\text{CO}_2}^\alpha \quad (7)$$

Assuming different reaction orders, the C_{CO_2} can be expressed as a function of time by integrating eqn (7). For the CaO model sorbent, a first-order kinetic was identified (eqn (8)). Noteworthily, other kinetic models for solid-state reaction, such as the Prout-Tompkins model,⁶⁰ geometrical contraction models, and diffusion models,⁶¹ which have been studied for the kinetics of thermal decomposition of CaCO₃,^{62,63} failed to fit the data obtained in this study.

$$C_{\text{CO}_2} = C_{\text{CO}_2,0} \exp \left[- (k_1 + k_2' + k_3') t \right] \quad (8)$$

Combining the rate equations (eqn (5) and (6)) with the expression of C_{CO_2} (eqn (8)), the rate (apparent) constant k for

the desorption of CO₂, CO, and CH₄ can be calculated based on eqn (9)–(11).

$$\ln r_{\text{CO}_2} = \ln k_1 + \ln C_{\text{CO}_2,0} - (k_1 + k_2' + k_3') t \quad (9)$$

$$\ln r_{\text{CO}} = \ln k_2' + \ln C_{\text{CO}_2,0} - (k_1 + k_2' + k_3') t \quad (10)$$

$$\ln r_{\text{CH}_4} = \ln k_3' + \ln C_{\text{CO}_2,0} - (k_1 + k_2' + k_3') t \quad (11)$$

The pure CaO sorbent was evaluated at different plasma powers and the developed kinetic model was evaluated using the resulting data. Fig. 5 shows the original data obtained over the CaO at different plasma powers. According to the Q – V Lissajous curve of the discharge (see Fig. 5(a)), the applied powers were 24.7, 26.4, and 28.3 W, respectively. As shown in Fig. 5(b)–(d), a small change in plasma power significantly influenced the desorption rate. The maximum rate of CO + CO₂ + CH₄ decreased from 525 to 239 and 152 $\mu\text{mol} (\text{g}^{-1} \cdot \text{min}^{-1})$ with decreasing plasma power from 28.3 to 26.4 and 24.7 W. Further decreasing power to below 23 W showed almost no activity, highlighting the importance of using plasma power that would allow for optimum material performance. Meanwhile, the FWHM and peak time increased with a decrease in desorption rate. As shown in Fig. 5(e), both FWHM and peak times increase almost linearly with decreasing plasma power from 28.3 to 24.7 W. Additionally, the influence of plasma power on the rates of CO and CO₂ desorption was quite different (see Fig. 5(c) and (d)), corresponding to a higher CO₂ conversion at lower power (see Fig. 5(f)). As the power decreased from 28.3 W to 26.4 and 24.7 W, CO₂ conversion increased from 70% to 84.6% (Fig. S8†) and 87.7% (Fig. S9†).

For the kinetic analysis, the normalized concentration of CO₂ remaining in the sorbent was calculated based on the amounts of CO, CO₂, and CH₄ desorbed (eqn (12)).

$$C_{\text{CO}_2} = 1 - \frac{\sum n_{i,(t)}}{\sum n_{i,(\text{total})}} \quad (12)$$

where $n_{i,(t)}$ is the cumulative desorption of CO, CO₂, and CH₄ at time t , and $n_{i,(\text{total})}$ is the cumulative total desorption of CO, CO₂, and CH₄.

The changes of C_{CO_2} with time were calculated using eqn (12) and the data are shown in Fig. 6(a) and (b). It was noticed that the $\ln (C_{\text{CO}_2})$ decreased linearly with time after reaching the maximum desorption rate, confirming the first-order desorption kinetics (eqn (8)). Noteworthily, before reaching the maximum desorption rate, the plasma reactor was still under a non-steady-state due to the changing of the reactor temperature; therefore, the relationship between C_{CO_2} and time deviated from the first-order kinetic behavior. The apparent rate constant k from the slope of the linear relationship represented the sum of the rate constants of reactions (i)–(iii), namely $k = k_1 + k_2' + k_3'$. The k -value could also be evaluated from the rates of CO and CO₂ desorption (after reaching the maximum rate) according to eqn (9) and (10). As shown in Fig. 6(b)–(d), the k -values obtained from the C_{CO_2} were similar to that obtained



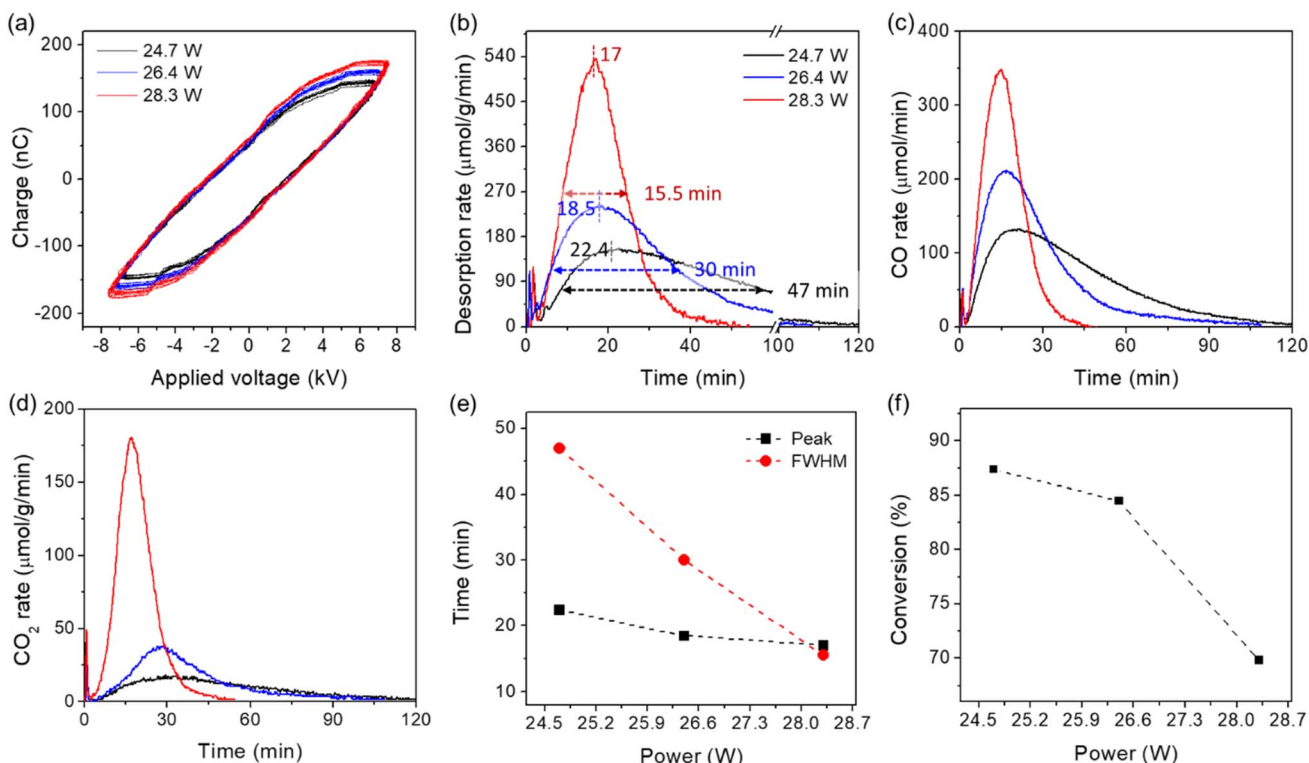


Fig. 5 Influence of plasma power on the reaction/desorption behaviors of CO_2 captured by CaO . (a) Q – V Lissajous curve of the discharge; (b)–(d) desorption rates of $\text{CO} + \text{CO}_2 + \text{CH}_4$, CO , and CO_2 , respectively, and (e) peak and FWHM times of the desorption rate, and (f) CO_2 conversion as a function of power. Reaction conditions: 0.1 g of "CaCO₃" (CaO after DAC for 24 h), 10% H₂/Ar 30 mL min⁻¹.

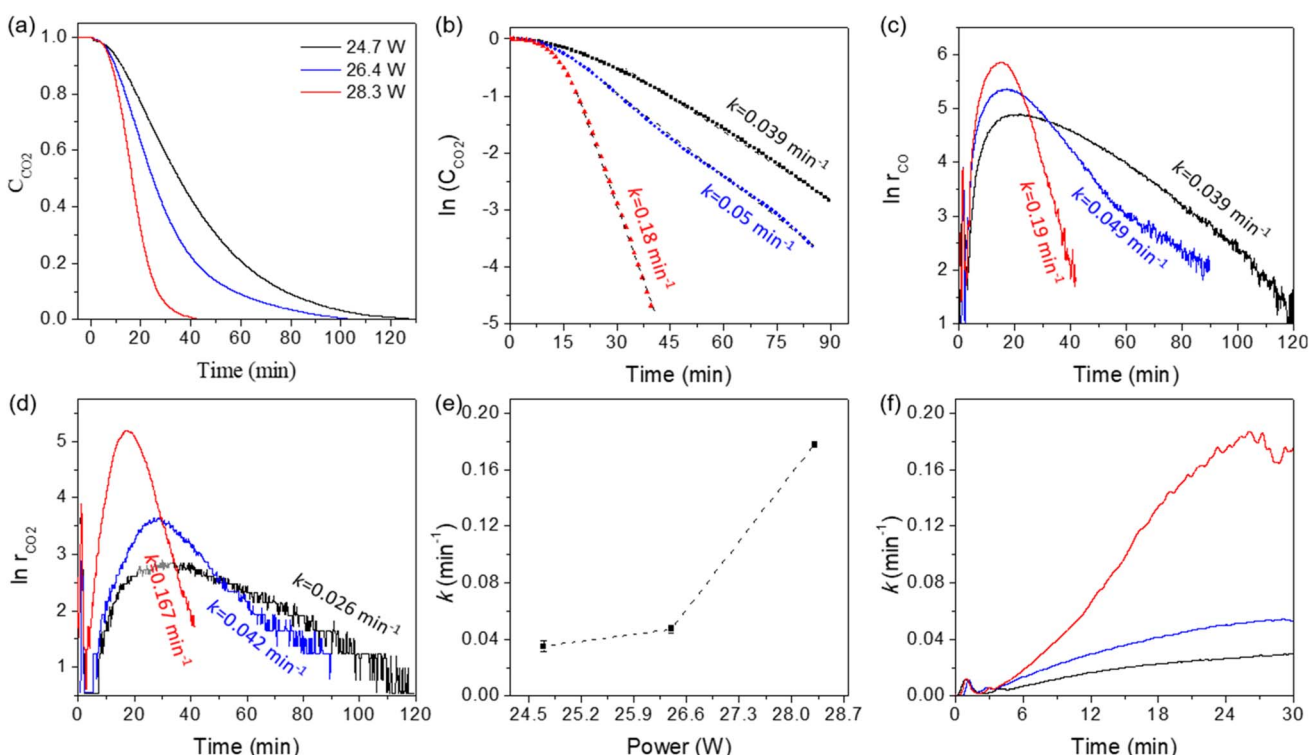


Fig. 6 Kinetic analysis of the data obtained at different plasma power. (a) Normalized CO_2 concentration (remaining in the sorbent) as a function of time (calculated using eqn (12)) (b) normalized CO_2 concentration modeled based on eqn (8); (c) rate of CO desorption modeled based on eqn (10); (d) rate of CO_2 desorption modeled based on eqn (9); (e) rate constant k as a function of plasma power; (f) changes in rate constant k before reaching a steady state.

from the rate of CO desorption, consistent with the developed model. However, the k -values obtained from the rate of CO_2 desorption were slightly lower than that obtained from the C_{CO_2} , which was probably due to the presence of gas phase reactions, such as CO_2 hydrogenation and splitting under plasma conditions.

While the rate constants k_1 and k'_1 from the eqn (9) and (10) could have been evaluated based on the intercept of the linear relationship between the rates of CO_2 and CO with time, such a calculation was found to be invalid, potentially due to the magnified error of the intercept by small changes in slope. Hence, the average k -values shown in Fig. 6(b)–(d) were replotted as a function of plasma power in Fig. 6(e). As shown in Fig. 6(e), the k -value increased significantly with increasing power. Besides the steady-state (after reaching the maximum rate of desorption) kinetics, the changes in k -value during the induction period can be obtained based on the differentiation of $\ln(C_{\text{CO}_2})$ with time (eqn (13)). As shown in Fig. 6(f), it was found that the k -value during the induction period increased, reaching a steady state after around 25–30 min, depending on the applied plasma power.

$$k = \frac{d \ln C_{\text{CO}_2}}{dt} \quad (13)$$

4. Conclusions

We showcase an electrified process (capable of using intermittent renewable energy) for the desorption and conversion of captured CO_2 from atmospheric air. Specifically, the CaO based sorbents can be employed for CO_2 direct air capture, and the desorption and conversion were achieved through solely nonthermal DBD plasma without additional heat supply. The efficiency of the proposed plasma-assisted process is extensively investigated based on the desorption rates of CO_2 , CO, and CH_4 , the conversion of CO_2 , as well as the selectivity of CO and CH_4 over the different CaO based sorbents. The desorption rates and CO_2 conversion depend highly on the plasma power and the composition of the sorbents. The desorption rate increases, but CO_2 conversion decreases with increasing power. CO_2 conversion is up to 87.7% with pure CaO as the sorbent under the discharge of 10% H_2/Ar at a power of 24.7 W. Meanwhile, introducing Ni to the CaO sorbent increased CO_2 conversion from 70 to 77% at a power of 28.3 W, and the rate of desorption was almost not influenced. In contrast, the metal oxide additives, such as MgO and ZrO_2 , decrease the desorption rates with only slightly increased CO_2 conversion. Additionally, the selectivity of CO and CH_4 could be tuned. Typically, more than 95% of CO selectivity could be obtained over the investigated sorbents. The formation of CH_4 can be maximized (selectivity of 94%) over the Ni-Ru CaO/ CeO_2 – Al_2O_3 dual function material, which can be achieved at a significantly lower plasma power. Moreover, the kinetics of such a plasma-assisted desorption and conversion process are evaluated based on the nonsteady-state semi-batch reactor model. The reactions are identified to be first-order for both CO_2 desorption and hydrogenation and the

rate constant is around 0.18 min^{-1} at a plasma power of 28.3 W. To summarize, this research shows the feasibility of employing DBD plasma for the desorption and conversion of CO_2 captured by CaO sorbent from the atmospheric air. This process can be coupled with Fischer–Tropsch synthesis, leading to a representative power-to-liquid process. With appropriate catalyst design, the process can also produce methane with high selectivity, known as the power-to-gas process. We suggest that future research should focus on the materials design to improve the desorption rate and CO_2 conversion, as well as CO or CH_4 selectivity optimization, and a fundamental understanding of the surface interaction mechanism between plasma-activated species and the sorbent is critical to material design.

Data availability

The data that support results from our work are available from the corresponding author.

Author contributions

Chinwendu Umeojiakor: investigation; data curation; writing—original draft. Loukia-Pantzechroula Merkouri: investigation; data curation; writing—original draft. Anthony Griffin: investigation; data curation; writing—original draft. Melis S. Duyar: conceptualization; supervision; writing—review and editing. Zhe Qiang: supervision; writing—review and editing. Yizhi Xiang: conceptualization; supervision; writing—review and editing.

Conflicts of interest

The authors declare no conflict of interest.

Acknowledgements

The DBD plasma reactor system was purchased with partial support from Ergon, Inc. Distinguished Professorship (Dr Neeraj Rai). C. U. acknowledged the financial support from Holly Construction Company for her PhD program. A. G. and Z. Q. acknowledged the partial financial support from U.S. National Science Foundation (CMMI-2239408). SASOL is kindly acknowledged for providing the CeO_2 – Al_2O_3 support. Financial support for this work was provided in part by the School of Chemistry and Chemical Engineering and the Doctoral College of the University of Surrey.

References

- <https://www.iea.org/reports/co2-emissions-in-2023/executive-summary>.
- <https://www.whitehouse.gov/wp-content/uploads/2021/10/US-Long-Term-Strategy.pdf>.
- F. Sabatino, M. Mehta, A. Grimm, M. Gazzani, F. Gallucci, G. J. Kramer and M. van Sint Annaland, *Ind. Eng. Chem. Res.*, 2020, **59**, 7007–7020.
- Q. Shu, L. Legrand, P. Kuntke, M. Tedesco and H. V. M. Hamelers, *Environ. Sci. Technol.*, 2020, **54**, 8990–8998.



5 W. H. Lee, X. Zhang, S. Banerjee, C. W. Jones, M. J. Realff and R. P. Lively, *Joule*, 2023, **7**, 1241–1259.

6 V. Nikulshina, C. Gebald and A. Steinfeld, *Chem. Eng. J.*, 2009, **146**, 244–248.

7 Y. Xu, S. J. Liu, J. P. Edwards, Y. C. Xiao, Y. Zhao, R. K. Miao, M. Y. Fan, Y. J. Chen, J. E. Huang, E. H. Sargent and D. Sinton, *Joule*, 2023, **7**, 2107–2117.

8 A. MacKenzie, D. L. Granatstein, E. J. Anthony and J. C. Abanades, *Energy Fuels*, 2007, **21**, 920–926.

9 M. T. Dunstan, F. Donat, A. H. Bork, C. P. Grey and C. R. Müller, *Chem. Rev.*, 2021, **121**, 12681–12745.

10 A. M. Kierzkowska, R. Pacciani and C. R. Müller, *ChemSusChem*, 2013, **6**, 1130–1148.

11 G. T. Rochelle, *Science*, 2009, **325**, 1652–1654.

12 D. P. Hanak, E. J. Anthony and V. Manovic, *Energy Environ. Sci.*, 2015, **8**, 2199–2249.

13 M. E. Boot-Handford, J. C. Abanades, E. J. Anthony, M. J. Blunt, S. Brandani, N. Mac Dowell, J. R. Fernández, M.-C. Ferrari, R. Gross, J. P. Hallett, R. S. Haszeldine, P. Heptonstall, A. Lyngfelt, Z. Makuch, E. Mangano, R. T. J. Porter, M. Pourkashanian, G. T. Rochelle, N. Shah, J. G. Yao and P. S. Fennell, *Energy Environ. Sci.*, 2014, **7**, 130–189.

14 M. A. Naeem, A. Armutlulu, Q. Imtiaz, F. Donat, R. Schäublin, A. Kierzkowska and C. R. Müller, *Nat. Commun.*, 2018, **9**, 2408.

15 K. S. Sultana, D. T. Tran, J. C. Walmsley, M. Rønning and D. Chen, *Ind. Eng. Chem. Res.*, 2015, **54**, 8929–8939.

16 M. Krödel, L. Abduly, M. Nadjafi, A. Kierzkowska, A. Yakimov, A. H. Bork, F. Donat, C. Copéret, P. M. Abdala and C. R. Müller, *Adv. Funct. Mater.*, 2023, **33**, 2302916.

17 H. Sun, J. Wang, X. Liu, B. Shen, C. M. A. Parlett, G. O. Adwek, E. John Anthony, P. T. Williams and C. Wu, *J. Mater. Chem. A*, 2019, **7**, 9977–9987.

18 H. J. Yoon and K. B. Lee, *Chem. Eng. J.*, 2019, **355**, 850–857.

19 L. P. Merkouri, J. L. Martin-Espejo, L. F. Bobadilla, J. A. Odriozola, A. Penkova, T. R. Reina and M. S. Duyar, *J. Mater. Chem. A*, 2023, **11**, 13209–13216.

20 L.-P. Merkouri, A. I. Paksoy, T. Ramirez Reina and M. S. Duyar, *ACS Catal.*, 2023, **13**, 7230–7242.

21 L.-P. Merkouri, T. Ramirez Reina and M. S. Duyar, *Nanoscale*, 2022, **14**, 12620–12637.

22 H. Sun, J. Wang, J. Zhao, B. Shen, J. Shi, J. Huang and C. Wu, *Appl. Catal., B*, 2019, **244**, 63–75.

23 M. Abdallah, Y. Lin and R. Farrauto, *Appl. Catal., B*, 2023, **339**, 123105.

24 S. Sun, C. Zhang, Y. Wang, X. Zhao, H. Sun and C. Wu, *Chem. Eng. J.*, 2023, **468**, 143712.

25 B. Shao, Z.-Q. Wang, X.-Q. Gong, H. Liu, F. Qian, P. Hu and J. Hu, *Nat. Commun.*, 2023, **14**, 996.

26 M. Erans, E. S. Sanz-Pérez, D. P. Hanak, Z. Clulow, D. M. Reiner and G. A. Mutch, *Energy Environ. Sci.*, 2022, **15**, 1360–1405.

27 M. Samari, F. Ridha, V. Manovic, A. Macchi and E. J. Anthony, *Mitig. Adapt. Strategies Glob. Change*, 2020, **25**, 25–41.

28 M.-H. Chang, C.-M. Huang, W.-H. Liu, W.-C. Chen, J.-Y. Cheng, W. Chen, T.-W. Wen, S. Ouyang, C.-H. Shen and H.-W. Hsu, *Chem. Eng. Technol.*, 2013, **36**, 1525–1532.

29 V. Nikulshina, D. Hirsch, M. Mazzotti and A. Steinfeld, *Energy*, 2006, **31**, 1715–1725.

30 V. Nikulshina, M. E. Gálvez and A. Steinfeld, *Chem. Eng. J.*, 2007, **129**, 75–83.

31 X. Tu, H. J. Gallon, M. V. Twigg, P. A. Gorry and J. C. Whitehead, *J. Phys. D: Appl. Phys.*, 2011, **44**, 274007.

32 X. Tu and J. C. Whitehead, *Appl. Catal., B*, 2012, **125**, 439–448.

33 X. Tu and J. C. Whitehead, *Int. J. Hydrogen Energy*, 2014, **39**, 9658–9669.

34 L. Wang, Y. Yi, C. Wu, H. Guo and X. Tu, *Angew. Chem., Int. Ed.*, 2017, **56**, 13679–13683.

35 H. Puliyalil, D. Lašić Jurković, V. D. B. C. Dasireddy and B. Likozar, *RSC Adv.*, 2018, **8**, 27481–27508.

36 J. A. Andersen, J. M. Christensen, M. Østberg, A. Bogaerts and A. D. Jensen, *Chem. Eng. J.*, 2020, **397**, 125519.

37 D. Li, V. Rohani, F. Fabry, A. Parakkulam Ramaswamy, M. Sennour and L. Fulcheri, *Appl. Catal., B*, 2020, **261**, 118228.

38 J. Feng, X. Sun, Z. Li, X. Hao, M. Fan, P. Ning and K. Li, *Adv. Sci. (Weinh.)*, 2022, **9**, e2203221.

39 T. Suttikul, S. Nuchdang, D. Rattanaphra, T. Photsathain and C. Phalakornkule, *Int. J. Hydrogen Energy*, 2022, **47**, 30830–30842.

40 M. Q. Feliz, I. Polaert, A. Ledoux, C. Fernandez and F. Azzolina-Jury, *J. Phys. D: Appl. Phys.*, 2021, **54**, 334003.

41 B. Ashford, C.-K. Poh, K. Ostrikov, L. Chen and X. Tu, *J. CO2 Util.*, 2022, **57**, 101882.

42 Y. Sun, J. Wu, Y. Wang, J. Li, N. Wang, J. Harding, S. Mo, L. Chen, P. Chen, M. Fu, D. Ye, J. Huang and X. Tu, *JACS Au*, 2022, **2**, 1800–1810.

43 J. Li, X. Zhai, C. Ma, S. Zhu, F. Yu, B. Dai, G. Ge and D. Yang, *Nanomaterials*, 2019, **9**, 1595.

44 V. Guerra, T. Silva, N. Pinhão, O. Guaitella, C. Guerra-Garcia, F. J. J. Peeters, M. N. Tsampas and M. C. M. van de Sanden, *J. Appl. Phys.*, 2022, **132**, 070902.

45 T. Kozák and A. Bogaerts, *Plasma Sources Sci. Technol.*, 2014, **23**, 045004.

46 R. Aerts, T. Martens and A. Bogaerts, *J. Phys. Chem. C*, 2012, **116**, 23257–23273.

47 S. Li, M. Ongis, G. Manzolini and F. Gallucci, *Chem. Eng. J.*, 2021, **410**, 128335.

48 S. Li, G. D. Felice, S. Eichkorn, T. Shao and F. Gallucci, *Plasma Sci. Technol.*, 2024, **26**, 094001.

49 M. R. Shawon, C. Umeojiakor, A. Griffin, J. Aguinaga, J. C. Wu, D. Patton, Z. Qiang, H. Toghiani and Y. Z. Xiang, *React. Chem. Eng.*, 2025, **10**, 320–331.

50 G. Chen, J. Qu, P. Cheah, D. Cao, Y. Zhao and Y. Xiang, *Ind. Eng. Chem. Res.*, 2022, **61**, 11436–11443.

51 J. Van, G. Chen and Y. Xiang, *Ind. Eng. Chem. Res.*, 2023, **62**, 2516–2524.

52 A. Griffin, G. Chen, M. Robertson, K. Wang, Y. Xiang and Z. Qiang, *ACS Omega*, 2023, **8**, 15781–15789.



53 T. Liang, H. Toghiani and Y. Xiang, *Ind. Eng. Chem. Res.*, 2018, **57**, 15301–15309.

54 S. Sun, Y. Wang, Y. Xu, H. Sun, X. Zhao, Y. Zhang, X. Yang, X. Bie, M. Wu, C. Zhang, Y. Zhu, Y. Xu, H. Zhou and C. Wu, *Appl. Catal., B*, 2024, **348**, 123838.

55 Z. Lv, T. Deng, C. Gao, Y. Zheng, C. Wu, J. Ran and C. Qin, *Chem. Eng. J.*, 2024, **489**, 151427.

56 L.-P. Merkouri, T. R. Reina and M. S. Duyar, *Energy Fuels*, 2021, **35**, 19859–19880.

57 A. Scaltsoyiannes and A. Lemonidou, *Chem. Eng. Sci.*, 2020, **8**, 100071.

58 C. Wang, H. Sun, X. Liu, X. Jin, Y. Feng, H. Shi, D. Wang, Y. Zhang, Y. Wang and Z. Yan, *Fuel*, 2023, **345**, 128238.

59 L.-P. Merkouri, L. F. Bobadilla, J. L. Martín-Espejo, J. A. Odriozola, A. Penkova, G. Torres-Sempere, M. Short, T. R. Reina and M. S. Duyar, *Appl. Catal., B*, 2025, **361**, 124610.

60 M. E. Brown, *Thermochim. Acta*, 1997, **300**, 93–106.

61 A. Khawam and D. R. Flanagan, *J. Phys. Chem. B*, 2006, **110**, 17315–17328.

62 I. Halikia, L. Zoumpoulakis, E. Christodoulou and D. Prattis, *ejmp&ep*, 2001, **1**, 89–102.

63 E. G. Calvo, M. A. Arranz and P. Letón, *Thermochim. Acta*, 1990, **170**, 7–11.

